RSC Advances

PAPER

View Article Online
View Journal | View Issue

Cite this: *RSC Adv.*, 2022, **12**, 14902

In situ fabrication of porous biochar reinforced $W_{18}O_{49}$ nanocomposite for methylene blue photodegradation

Yi Li,[a] Wenting Chen,[a] Zhiwei Liu,[a] Dehua Cao,[a] Yu Chen,[b] Kunyapat Thummavichai,[b] Nannan Wang *[a] and Yanqiu Zhu *[ab]

In this paper, a novel cow dung based activated carbon (CDAC) was successfully modified by $W_{18}O_{49}$ nanowires as a photocatalyst using KOH activation and a hydrothermal method. The activity of photocatalytic degradation of methylene blue (MB) under full-spectrum light illumination shows great improvement, and the degradation rate of MB could reach 98% after 240 min (67% for $W_{18}O_{49}$), with a final degradation rate of 98%. The porous structure with specific surface area of CDAC (~479 m^2 g^{-1}) increases the adsorption of $W_{18}O_{49}$ reactants and also raises the concentration of reactants in the photocatalytic region. The high electrical conductivity and good electron storage capacity of CDAC allow the electrons excited in the conduction band (CB) of $W_{18}O_{49}$ to migrate smoothly into CDAC, which are the keys to enhancing the photocatalytic activity. Moreover, the photocatalytic mechanism was proposed. The results show that the CDAC/$W_{18}O_{49}$ nanowire composite can be used as an efficient photocatalyst for removal of MB dye from wastewater and indicate remarkable future potential in dye wastewater treatment technologies.

Received 8th April 2022
Accepted 10th May 2022

DOI: 10.1039/d2ra02280j

rsc.li/rsc-advances

1. Introduction

With the rapid development of industrial processes, the problem of environmental pollution is receiving more and more attention. For a long time, many kinds of organic dyes have been widely used in various industries, such as tanneries, and paper and textile production,[1,2] and the wastewater produced during their production is the main source of dye pollution in water bodies.[3–6] Even low concentrations of dyes can cause great harm to humans, for example, methylene blue (MB) can cause serious skin problems, chromosome breakage, mutagenesis and human respiratory toxicity.[6–8] Therefore, the challenge of how to remove organic dyes from wastewater has attracted widespread interest in the community.

To date, several techniques have been developed to address organic dyes in wastewater, such as solvent extraction, chemical oxidation, photocatalytic degradation, biodegradation, and adsorption.[9–15] Among them, photocatalysis is a green, effective, environmentally friendly and highly promising advanced oxidation process for wastewater treatment, which uses semiconductor materials and light to remove organic pollutants. Tungsten oxide (WO_{3-x}, $0 \leq x \leq 1$), a semiconductor material has the advantages of narrow band gap (range of 2.4 to 3.0 eV) favorable for visible light absorption, deep valence band for oxidation reaction, high carrier mobility and good stability.[16–19] This makes WO_{3-x} a favorable candidate for solar-driven chemical reactions. Among them, non-stoichiometric $W_{18}O_{49}$ structure is rich in W^{5+} defects and oxygen vacancies, which can be used as reaction sites to facilitate the adsorption and activation of oxygen molecules, hence it has a significant important for the development of efficient photocatalysts for the removal of organic dyes from water.[20,21]

Unfortunately, the efficiency of narrow bandgap photocatalysts is relatively low due to the fast-compounding efficiency of photogenerated charge carriers, which inhibits the migration of these charges to reach the semiconductor surface to participate in redox reactions. In addition, their photostability is easily compromised because the oxidation and/or reduction potentials tend to lie within the band levels that induce photooxidation and/or reduction.[22] For $W_{18}O_{49}$, it is easily deactive during photocatalysis due to the formation of WO_3 by photooxidation of holes accumulated in the valence band.[21] Therefore, the photocatalytic activity of most single-component photocatalysts is still far from satisfactory.[23]

In recent years, carbon-based-tungsten oxide composites have been studied more frequently to effectively improve the light-driven performance of $W_{18}O_{49}$ by taking advantage of the large specific surface area, flexible structure, excellent charge carrier mobility, and good electrical and thermal conductivity of

[a]*Guangxi Institute Fullerene Technology (GIFT), Key Laboratory of New Processing Technology for Nonferrous Metals and Materials, Ministry of Education, School of Resources, Environment and Materials, Guangxi University, Nanning, 530004, China. E-mail: wangnannan@gxu.edu.cn; Y.zhu@exeter.ac.uk*

[b]*College of Engineering, Mathematics and Physical Sciences, University of Exeter, Exeter, EX4 4QF, UK*

carbon-based materials.[24,25] Yang *et al.* reported a composite of highly ordered mesoporous WO_3 nanocrystals grown on RGO, which was used as visible-light-driven photocatalyst for oxygen production. Under visible light irradiation, the amount of oxygen evolution from the optimized photocatalyst containing *ca.* 6 wt% RGO reached 437.3 μmol g^{-1}, which was 5.1 times as high as that from m-WO_3.[26] Li *et al.* synthesized a lightweight 3-D porous aerogel using one-dimensional tungsten oxide nanowires and two-dimensional reduced graphene oxide sheets, and investigated the photocatalytic activity of the aerogel under visible light irradiation by degrading six different organic dyes.[18] Deng *et al.* reported a rationally designed novel layered $W_{18}O_{49}$/g-C_3N_4 composite with enhanced photocatalytic activity by controlling the flow of dual-channel charge carrier separation and transfer processes, and the prepared composite exhibited enhanced photocatalytic performance under both full-spectrum light and near-infrared (NIR) light irradiation due to an effective strategy combining morphological structure and energy band structure modulation. Under optimal conditions, the degradation rate of $W_{18}O_{49}$/g-C_3N_4 composites to MB was 0.0677 min^{-1}, which was 3 times and 5 times of g-C_3N_4(0.0276 min^{-1}) and $W_{18}O_{49}$(0.0148 min^{-1}), respectively; the removal of CIP by the $W_{18}O_{49}$/g-C_3N_4 composite reached 93.5% under full spectrum light (λ > 365 nm) irradiation for 120 min. For g-C_3N_4 and $W_{18}O_{49}$, 69.2% and 53.8% of CIP could be removed under the same conditions.[16]

Biochar is a cheap and green carbon-based material obtained by pyrolysis of biomass feedstock at high temperatures and under anaerobic conditions.[27] Biochar has a high surface area and porous structure, structural defect sites and various surface functional groups, which provide excellent electrical conductivity and electron storage capacity in photocatalytic processes.[28] Electrons that leap under light can be transferred to biochar, contributing to a lower electron–hole complexation rate in the photocatalytic process, which improves the oxidative removal of target compounds, while the raw material is renewable and easily available.[29,30] Cow dung is a common livestock waste product, which is mainly derived from undigested cellulose-based feed residues and without proper treatment will cause environmental problems such as deterioration of air quality, public hazards (*e.g.*, infectious pathogens and asphyxiation poisoning), greenhouse gas emissions, and water pollution.[31] Currently, cattle manure is used by some as cooking fuel, disinfectant cleaner, construction material, insulation material, waterproofing material for walls and floors of rural houses, and for electricity generation. There is also the use of cattle manure as a raw material for the preparation of biochar, which can be an effective solution for a large amount of livestock waste.[32,33] Thus, cattle manure can be used as a cheap and abundant source of carbon material.

In this paper, high specific surface area porous structure cow dung active carbon (CDAC) was prepared for the first time by using cow dung as carbon raw material and active by KOH, and $W_{18}O_{49}$ was loaded on CDAC by hydrothermal method to synthesize CDAC/$W_{18}O_{49}$ composites, which benefited from the large specific surface area structure of CDAC and the interface between amorphous carbon CDAC and $W_{18}O_{49}$ could extend the current The photocatalytic degradation of MB by CDAC/$W_{18}O_{49}$ composites was enhanced by the large surface area structure of CDAC and the interface between amorphous carbon CDAC and $W_{18}O_{49}$, which could extend the current carrier lifetime and accelerate the charge transfer. In addition, a schematic diagram of the reaction mechanism was constructed, and a possible photocatalytic mechanism was proposed.

2. Experimental section

2.1. Materials

Cow dung was obtained from Guangxi Buffalo Research Institute (Nanning, China). Tungsten hexachloride (WCl_6), cyclohexanol and methylene blue (MB) were purchased from Shanghai Macklin Biochemical Co. Potassium hydroxide (KOH), disodium EDTA-2Na, anhydrous ethanol, *tert*-butanol (*t*-BuOH), hydrochloric acid (HCl) and 1,4-benzoquinone (BQ) were purchased from Guandong Guanghua Sci-Tech Co. Deionized (Dl) water was obtained from an ultrapure water production facility and used throughout the experiments. All chemicals and reagents were used as received without further purification.

2.2. Preparation of the cow dung active carbon

CDAC was synthesized by chemical activation using KOH as the activator and pre-carbonized cow dung charcoal as the precursor. First, the sun-dried cow dung was pre-carbonized in the tube furnace at 450 °C for 2 h under an argon gas flow rate of 50 ml min^{-1}. Then, the charcoal was mixed with KOH in a 1 : 2 ratio. The mixture was transferred to an alumina crucible and pyrolyzed at a rate of 10 °C min^{-1} in a constant stream of argon at 800 °C, and then held for 2 h before natural cooling. The obtained product was washed with 1.0 M hydrochloric acid to remove residual KOH, followed by DI water until the filtrate became neutral. Finally, the fabricated CDAC was collected after drying at 80 °C overnight.[32]

2.3. Preparation of the CDAC/$W_{18}O_{49}$ composite

Firstly, 40 mg of CDAC obtained was added to 70 ml of cyclohexanol solution and stirred at 40 °C for 1 h to obtain a homogeneous mixture. Then, 83.3 mg of WCl_6 was dissolved in 70 ml of the mixed solution and kept stirring for 15 min. Then mixture was sealed in an autoclave with a Teflon liner and heated at 200 °C for 6 h. Finally, the black-blue precipitate was collected by centrifugation, washed several times with ethanol and deionized water, and dried in vacuum at 60 °C for 10 h. For comparison, pure $W_{18}O_{49}$ was also synthesized in the same way, without the addition of CDAC.

2.4. Characterization of materials

The crystal structure of the catalysts was characterized with Cu Kα1 radiation (λ = 1.54056 Å) using an X-ray diffractometer (XRD, Rigaku D/MAX 2500 V, Rigaku Corporation) at an accelerating voltage of 45 kV, scan rate (2θ): 0.05° s^{-1}, recording a 2θ range of 10° to 80°. Scanning electron microscopy (SEM, Sigma 300, Carl Zeiss) was used to study the microstructure and

morphology of the prepared photocatalysts. The FT-IR of the synthesized photocatalysts was collected by transmission electron microscopy (TEM) and high-resolution transmission electron microscopy (HR-TEM) (F20 S-TWIN electron microscope, Tecnai G2, FEI Co.) at an accelerating voltage of 200 kV. FT-IR spectra of the synthesized photocatalysts were collected by Fourier transform infrared spectrometer (IRAffinity-1, Shimadzu, Japan). A surface area analyzer (TriStar II 3020, Micromeritics) was used to analyze the specific surface area and pore volume of the synthesized photocatalysts. To obtain Raman spectra, a microscopic Raman spectrometer (HORIBA Jobin Yvon, Lab RAM HR Evolution) with Raman shifts measured between 100 cm^{-1} and 2000 cm^{-1} was used. X-ray photoelectron spectroscopy (XPS) of the prepared samples was performed on an XPS spectrometer with Al Kα source (XPS, ESCALAB 250XI, Thermo Fisher), exploring the valence states of W and C elements in the prepared samples. The UV-vis-NIR diffuse reflectance spectra (UV-vis-NIR DRS) of the prepared samples were performed by an UV-vis-NIR spectrophotometer equipped with an integrating sphere (PerkinElmer LAMBDA 365 UV/Vis Spectrophotometer) using $BaSO_4$ as a reference.

2.5. Photoelectrochemical measurement

A typical three-electrode measurement system based on the CHI 660D workstation was applied to measure the photoelectrochemical properties of the as-prepared samples. Pt electrode and an Ag/AgCl electrode in saturated KCl solution were used as counter electrode and reference electrode, respectively. The photocurrent density was measured in a 1 M sulfuric acid electrolyte solution under visible light provided by a 300 W Xe arc lamp ($\lambda > 365$ nm). Electrochemical impedance spectroscopy (EIS) was measured based on the photoelectrochemical test system described above.

2.6. Photocatalytic activity measurement

The photocatalytic activity of the prepared photocatalysts was investigated by degrading MB under light irradiation. A 300 W xenon lamp (PLS/SXE 300C, Perfectlight Co., Ltd, Beijing) was employed as the light source, and it was directly used as a full-spectrum light source without any filter. Before the photocatalytic experiment started, 10 mg of the prepared photocatalyst was added into 100 mL of 35 mg L^{-1} MB aqueous solution and stirred for 60 min to reach the adsorption equilibrium under protection from light. During the photocatalytic process, the quantitative aqueous solution was collected at certain time intervals, and the photocatalyst was removed by centrifugation and analyzed.

3. Results and discussions

3.1. Structure and morphology characteristics

Fig. 1 shows two diffraction peaks are observed at 25° and 43° for cow dung active carbon, corresponding to the graphitic phase structure on the (002) plane and the chaotic carbon layer structure on the (101) plane. The spectra of $W_{18}O_{49}$ nanowires show characteristic peaks at 23.4°,25.8°, 34.9°, 47.8° and 55.6°

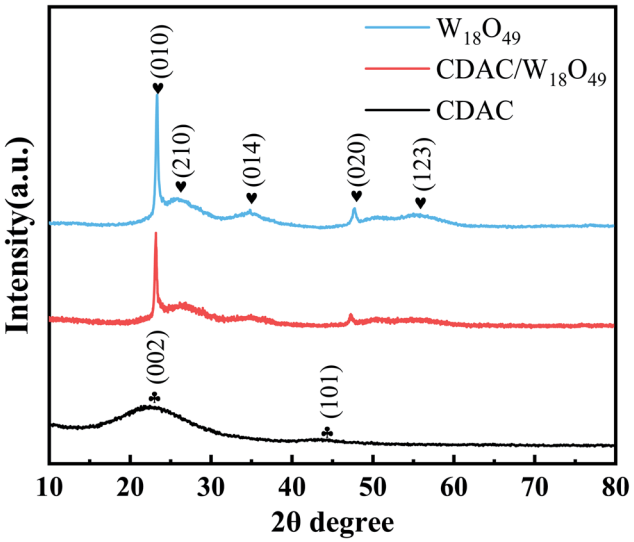

Fig. 1 XRD patterns of the prepared CDAC, $W_{18}O_{49}$ and CDAC/$W_{18}O_{49}$.

positions corresponding to (010), (210), (014), (020) and (123) crystallographic planes, respectively, which can be well matched with JCPDS No. 05-0392 (monoclinic $W_{18}O_{49}$) card, with (reported) The peak positions are consistent.[25] Although most of the diffraction peaks of CDAC/$W_{18}O_{49}$ composites correspond to the characteristic peaks of the monoclinic system $W_{18}O_{49}$, it can also be seen that the characteristic peaks of CDAC/$W_{18}O_{49}$ composites are shifted to the lower 2θ side compared to $W_{18}O_{49}$, which may be due to the lattice expansion when $W_{18}O_{49}$ forms composites with CDAC further supporting the high concentration of oxygen in the nanocomposites high concentration of vacancies; meanwhile, it can be observed that the characteristic peaks of CDAC in CDAC/$W_{18}O_{49}$ composites are not obvious, which may be caused by the low CDAC content and the poor crystallinity of CDAC/$W_{18}O_{49}$ composites. In addition, no peaks of other impurities were detected in the XRD patterns of the CDAC/$W_{18}O_{49}$ composites.

The surface morphology of the catalysts was investigated by SEM and TEM. Fig. 2a shows SEM image of pristine CDAC shows a rough surface filled with porous morphology. After passing the hydrothermal reaction, the surfaces of CDAC are modified with linear $W_{18}O_{49}$ (as in Fig. 2b). Further observation by higher magnification SEM images (Fig. 2c and d) shows that the $W_{18}O_{49}$ nanowires on CDAC have diameters of 20–60 nm and lengths of 0.3–0.8 μm. Fig. 2e represents transmission electron microscopy (TEM) images of individual CDAC/$W_{18}O_{49}$ composites, which can be seen to be modified with uniformly sized. Fig. 2f shows elemental mapping image of the CDAC/$W_{18}O_{49}$ composite shows that the C elements are mainly distributed in the middle region, while the O and W elements are mainly distributed on the outer surface of the C elements. HRTEM image (Fig. 2g) shows that the lattice stripe spacing of $W_{18}O_{49}$ nanowires on the surface of CDAC is ~0.38 nm, which is consistent with the lattice spacing of the (010) crystal plane of monoclinic $W_{18}O_{49}$, indicating that $W_{18}O_{49}$ grows along the (010) direction.

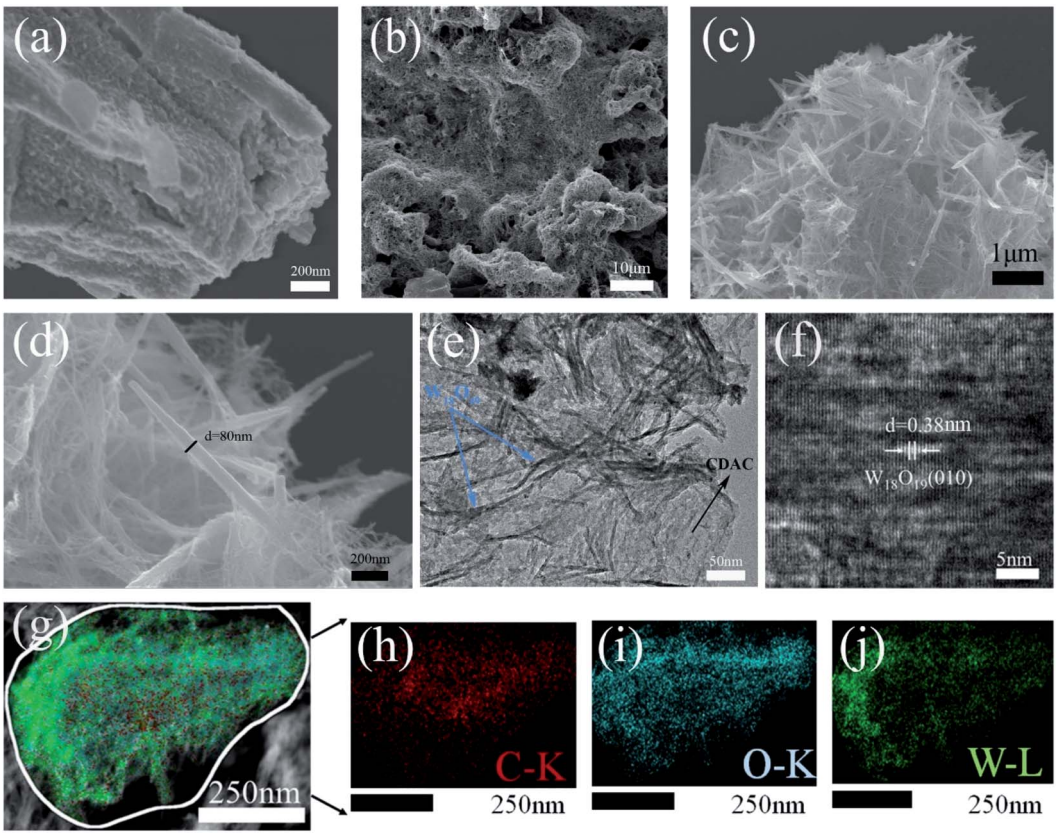

Fig. 2 SEM images of (a) CDAC (b–d) CDAC/W18O49 (e and f) TEM image of CDAC/W18O49 (g) the corresponding elemental mapping images of CDAC/W18O49 composites and (h–j) corresponding EDS mapping image of C, O and W element.

3.2. Specific surface area measurement

The pore structures and SSA of the materials CDAC, $W_{18}O_{49}$, and CDAC/$W_{18}O_{49}$ were analyzed by the adsorption and desorption of N_2. The N_2 adsorption and desorption curves of CDAC, $W_{18}O_{49}$, and CDAC/$W_{18}O_{49}$ composites are shown in Fig. 3. According to the classification criteria of the International Society for Pristine and Applied Chemistry, the curves can be classified as a combination of Class I and IV curves.[34] At relative pressures $P/P_0 < 0.1$, the CDAC and CDAC/$W_{18}O_{49}$ curves show a significant increase in N_2 adsorption, indicating the presence of a large number of micropores in the material, and at relative pressures in the range of $0.41 < P/P_0 < 0.95$, there is a significant hysteresis loop in both curves, indicating the presence of mesopores in the material, but the adsorption and desorption curves of $W_{18}O_{49}$ are not significant. When the relative pressure was in the range of $P/P_0 > 0.95$, the adsorption and desorption curves were close to vertical, suggesting the presence of macroporosity in all three materials. In addition, the SSA of CDAC is 479.1034 $m^2\ g^{-1}$, which is larger than that of CDAC/$W_{18}O_{49}$, but the relative pore volume is smaller than that of CDAC/$W_{18}O_{49}$, as shown in Table 1, which may be caused by the larger number of mesopores in CDAC and the larger number of macropores in CDAC/$W_{18}O_{49}$, which is consistent with the adsorption–desorption curve. The larger pore volume is beneficial to promote the photocatalytic effect of CDAC/$W_{18}O_{49}$ on MB.

3.3. Surface chemical composition and group analysis

Fig. 4a shows the Raman spectra of CDAC/$W_{18}O_{49}$ composites compared with the Raman spectra of CDAC and $W_{18}O_{49}$ nanowires. CDAC has two broad peaks at 1351 and 1595 cm^{-1} corresponding to the hybridized carbon atoms assigned to sp^3 (D-

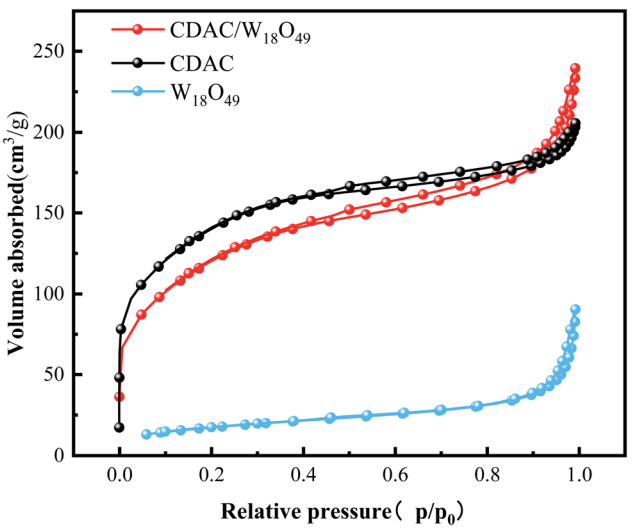

Fig. 3 N_2 adsorption–desorption isotherm of CDAC, $W_{18}O_{49}$, CDAC/$W_{18}O_{49}$ composites.

Table 1 Specific surface area and pore volume of the as-prepared samples

Samples	Specific surface area (SSA) ($m^2\ g^{-1}$)	Pore volume ($cm^3\ g^{-1}$)
CDAC/$W_{18}O_{49}$	422.1559	0.355
CDAC	479.1034	0.312
$W_{18}O_{49}$	59.2412	0.123

band) and sp^2 (G-band), respectively.[35] The Raman spectra of $W_{18}O_{49}$ nanowires is dominated by four major vibrational peaks at 252, 327, 717 and 788 cm^{-1}, attributed to the bending vibration of monoclinic phase $W_{18}O_{49}$ δ (O–W–O) and the stretching vibration of ν (W–O–W), respectively.[36] The Raman spectra of the CDAC/$W_{18}O_{49}$ composites show that they are comparable to the CDAC and $W_{18}O_{49}$ nanowires corresponding to the characteristic Raman peaks of the nanowires.

To further investigate the atomic structure of the CDAC/$W_{18}O_{49}$ composite, FT-IR tests were performed, as shown in Fig. 4d. There are five peaks in the spectrum of CDAC, the peak at 460 cm^{-1} is attributed to Si–O–Si bending vibration, the peak at 1085 cm^{-1} is attributed to C–C stretching vibration, the peaks at 1212 and 3428 cm^{-1} are attributed to the –OH stretching mode, and the peak at 1383 cm^{-1} is attributed to the medium C–O bond axial deformation vibration. –OH stretching mode, and the peak at 1383 cm^{-1} are an axial deformation vibration in the C–O bond. Characteristic stretching vibrational bands belonging to W=O and O–W–O (500–1000 cm^{-1}) are observed in the FTIR spectra of the $W_{18}O_{49}$ nanowire. After introducing $W_{18}O_{49}$ nanowires into CDAC, their FTIR spectra reveal the characteristic peaks of $W_{18}O_{49}$ nanowires and CDAC.

X-ray photoelectron spectra (XPS) spectra of the prepared samples are also provided to further investigate the interactions between CDAC and $W_{18}O_{49}$. The XPS spectra in Fig. 5a show that the prepared CDAC/$W_{18}O_{49}$ composites are mainly composed of C, W and O elements. Fig. 5b–d show the high-resolution spectra of C 1s, W 4f and O 1s. As shown in the high-resolution C 1s spectrum of CDAC in Fig. 5b, the peak at the binding energy of 284.80 eV is mainly attributed to C–C of surface amorphous carbon, while the peaks at 286.45 and 289.15 eV are attributed to C=O and O–C=O, respectively.[37] These three peaks can also be observed on the curves of CDAC/$W_{18}O_{49}$ samples. However, unlike the pure CDAC, the characteristic peaks of C=O and O–C=O in CDAC/$W_{18}O_{49}$ are shifted to the side with lower binding energy after adhering to the $W_{18}O_{49}$ nanowire. In the W 4f high-resolution XPS spectrum of pure $W_{18}O_{49}$ (Fig. 4a), the main spectrum is divided into two pairs of peaks, which represent two different oxidation states of element W, namely W^{6+} and W^{5+}. In the W 4f high-resolution XPS spectrum of pure $W_{18}O_{49}$ (Fig. 5c), the main spectrum is divided into two pairs of peaks, which represent two different oxidation states of element W, namely W^{6+} and W^{5+}. In the W 4f high-resolution XPS spectrum of pure $W_{18}O_{49}$ (Fig. 5c), the main spectrum is divided into two pairs of peaks, which represent two different oxidation states of element W, namely W^{6+} and W^{5+}. The peaks with binding energies of 36.20 and 38.30 eV can correspond to the W $4f_{7/2}$ and W $4f_{5/2}$ characteristic peaks of W^{6+}, respectively. The second double peak, with binding energies of 35.60 and 37.70 eV, corresponds to the W $4f_{7/2}$ and W $4f_{5/2}$ characteristic peaks of W^{5+}. In addition, it can be seen that the W 4f high-resolution XPS spectrum of CDAC/$W_{18}O_{49}$ exhibits a similar peak to the pure $W_{18}O_{49}$ spectrum with a slight offset. The position of the W 4f peak of CDAC/$W_{18}O_{49}$ is shifted toward higher binding energy values compared to pure $W_{18}O_{49}$, which can be attributed to the interaction between $W_{18}O_{49}$ and CDAC.[38] In the O 1s high-resolution XPS spectrum of $W_{18}O_{49}$ (Fig. 5d), the peaks located at 530.62, 531.34 and 531.95 eV are attributed to W–O, oxygen vacancy (O_v) and –OH, respectively, and the characteristic peaks of W–O, oxygen vacancy (O_v) and –OH are shifted to the higher binding energy side after the composite formation with CDAC. Notably, a new peak appears at 533.41 eV on the O 1s spectrum of the CDAC/W18O49 sample, which may be related to the C–O bonding because of the close contact and reaction between the CDAC and $W_{18}O_{49}$ nanowires. The shift of the binding energy on the XPS curve indicates the electron migration between $W_{18}O_{49}$ and CDAC, due to their different electron concentrations, electrons

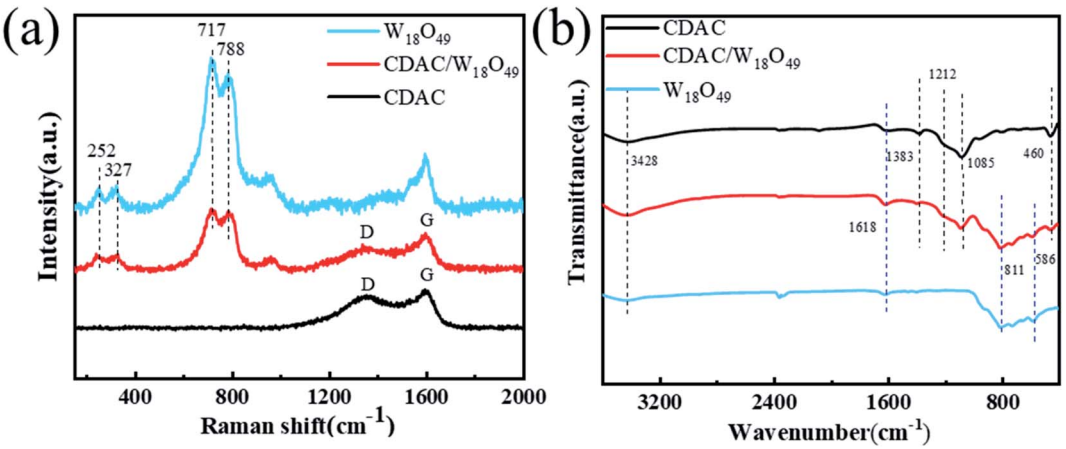

Fig. 4 (a) Raman spectra of prepared CDAC, $W_{18}O_{49}$ and CDAC/$W_{18}O_{49}$; (b) FT-IR spectra of CDAC, $W_{18}O_{49}$ and CDAC/$W_{18}O_{49}$.

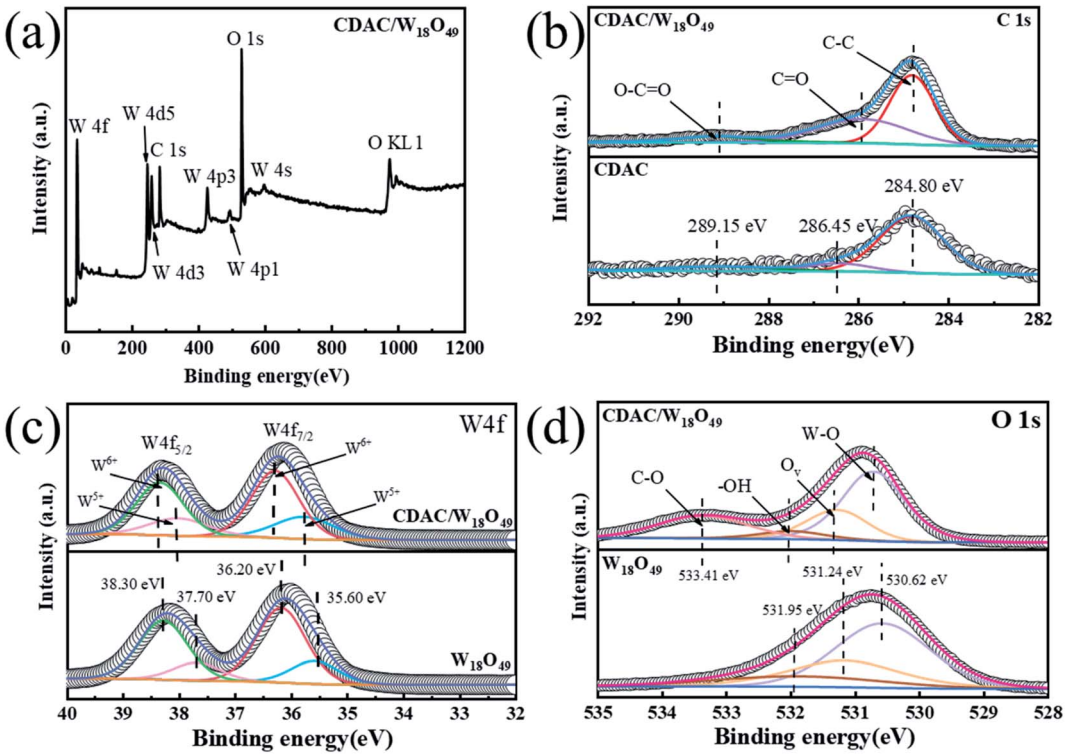

Fig. 5 The XPS spectra of the prepared CDAC/$W_{18}O_{49}$, $W_{18}O_{49}$ and CDAC: (a) survey, (b) C 1s, (c) W 4f, (d) O 1s.

are more willing to transfer from $W_{18}O_{49}$ nanowires to CDAC.[39] Based on the above analysis results, it can be confident that the $W_{18}O_{49}$ nanowires have been successfully assembled onto the CDAC.

3.4. Optical properties

The light trapping ability of CDAC, pristine $W_{18}O_{49}$ nanowires and CDAC/$W_{18}O_{49}$ composites was investigated by UV-vis-NIR absorption spectroscopy, and the relevant results are shown in the Fig. 6a. For CDAC showed significant absorption within the full spectrum.[40] The pristine $W_{18}O_{49}$ nanowires have a primary absorption edge of 440 nm and an absorption region ranging from 440 to 1100 nm, showing strong responsiveness throughout the visible region and near-infrared light range. This unique light absorption ability originates from the metal-like LSPR effect of the $W_{18}O_{49}$ nanowires due to the presence of abundant oxygen vacancies.[41,42] When CDAC was compounded with $W_{18}O_{49}$ nanowires, it was seen that the CDAC/$W_{18}O_{49}$ composites exhibited significant absorbance and a main absorption edge consistent with that of pristine $W_{18}O_{49}$ nanowires, further confirming the presence of $W_{18}O_{49}$ nanowires.

To fully understand the variation in light absorption capacity, the band gaps (E_g) of the $W_{18}O_{49}$ nanowires and CDAC/$W_{18}O_{49}$ composites were calculated by the following equation.[23]

$$\alpha h\nu = A(h\nu - E_g)^{n/2} \quad (1)$$

where α, h, ν, E_g and A are the absorption coefficient, Planck's constant optical frequency, band gap energy and constant,

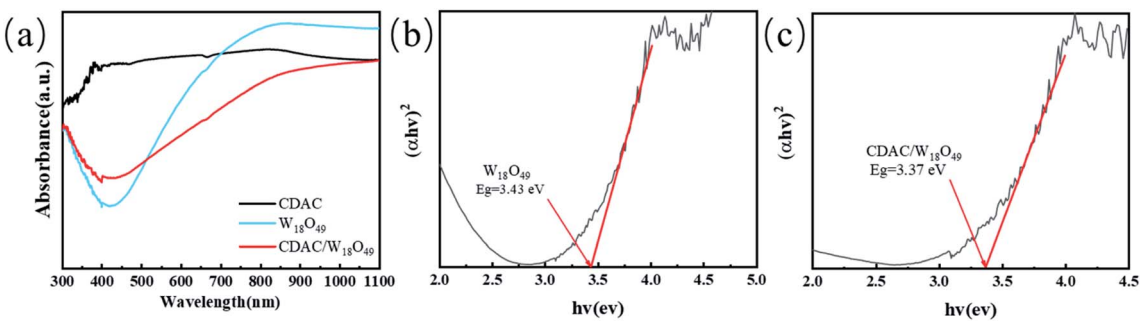

Fig. 6 (a) UV-vis-NIR diffuse reflectance spectra of the prepared CDAC, $W_{18}O_{49}$, and CDAC/$W_{18}O_{49}$; (b and c) the band gap energy of $W_{18}O_{49}$ and CDAC/$W_{18}O_{49}$.

respectively. Based on the results shown Fig. 6b and c, the $W_{18}O_{49}$ nanowire and CDAC/$W_{18}O_{49}$ composite are estimated to be 3.43 and 3.37 eV, respectively.

3.5. Photogenerated charge transport properties and transfer properties

To comprehensively investigate the photocurrent response and photogenerated charges compounding efficiency of the photocatalysts, transient photocurrent (It) and electrochemical impedance spectroscopy (EIS) were used to measure the charge transfer of the materials. The CDAC/$W_{18}O_{49}$ composite and $W_{18}O_{49}$ nanowires exhibited a significant photocurrent response during light irradiation in Fig. 7a. The CDAC/$W_{18}O_{49}$ composite exhibited a higher photocurrent density than that of the $W_{18}O_{49}$ nanowires, showing higher light trapping and lower photogenerated charge complexation efficiency, while the pristine CDAC showed no photocurrent response. EIS is an effective electrochemical approach to explain the electron transfer efficiency of the photocatalyst. Fig. 7b shows that the CDAC/$W_{18}O_{49}$ composite possesses the smallest diameter, which implies the lowest charge transfer impedance and complexation efficiency of photogenerated charges.

3.6. Photocatalytic activity of the prepared photocatalysts

The photocatalytic performance of the prepared CDAC/$W_{18}O_{49}$ composites was investigated by the degradation of methylene blue (MB). Adsorption experiments were performed under dark conditions prior to the photocatalytic degradation process to investigate the adsorption capacity of different photocatalysts. The results showed that the adsorption–desorption equilibrium between the photocatalyst and the pollutant molecules could be achieved within 60 min. Fig. 8a shows the MB degradation results for pristine $W_{18}O_{49}$ nanowires, CDAC and CDAC/$W_{18}O_{49}$ composites. The results show that for pristine $W_{18}O_{49}$ nanowires, only 67% of MB was degraded after 240 min of full spectrum irradiation (λ > 365 nm), while for CDAC, only 80% of MB was removed. When the prepared CDAC/$W_{18}O_{49}$ composites were added to the reaction system, the photocatalytic removal efficiency was improved. In Fig. 8a, it can be observed that the CDAC/$W_{18}O_{49}$ composite has the highest photocatalytic activity and can degrade 90% of MB molecules at 120 min of light, and the removal rate can reach 98% after 240 min. The better photocatalytic activity of CDAC/$W_{18}O_{49}$ composites may be attributed to the good electrical conductivity of CDAC as an electron absorber and transport network, the increased specific surface area of the composites with CDAC as a substrate, which allows more exposed active sites, and the lower band gap of $W_{18}O_{49}$ nanowires and the defect structure caused by numerous oxygen vacancies.

In addition, the kinetics of photocatalytic degradation of MB under full-spectrum light irradiation was investigated, and the results showed that the variation of MB concentration *versus* reaction time on CDAC/$W_{18}O_{49}$ composites followed a pseudo-first-order kinetic diagram with the equation $-\ln(C/C_0) = kt$, where t, C_0 and C are the reaction time, initial methyl concentration (mg L^{-1}), and methyl at time t, respectively concentration (mg L^{-1}). k represents the apparent pseudo primary rate constant (min^{-1}). The pseudo primary rate constants of pristine $W_{18}O_{49}$ nanowires, CDAC/$W_{18}O_{49}$ composites and CDAC are 0.00349, 0.01159 and 0.00463 min^{-1}, respectively, as can be seen in Fig. 8b. The pseudo primary rate constants of CDAC/$W_{18}O_{49}$ composites are higher than those of pristine $W_{18}O_{49}$ nanowires and CDAC, respectively. $W_{18}O_{49}$ nanowires and CDAC by a factor of about 3.3 and 2.5, respectively.

For practical applications, the reusability and stability of photocatalysts are very important, therefore, to evaluate the photostability of CDAC/$W_{18}O_{49}$ composites, cycling reactions were performed. After each catalytic run, the photocatalyst was separated from the solution, washed with ethanol and vacuum dried to ensure the purity of the recovered catalyst. As shown in Fig. 9, after five cycling experiments, the photocatalytic activity of CDAC/$W_{18}O_{49}$ did not show a significant degradation process, indicating that the prepared CDAC/$W_{18}O_{49}$ composites have high stability.

3.7. Photocatalytic reaction mechanism

In order to understand the photocatalytic mechanism of this composite, controlled experiments were performed to capture

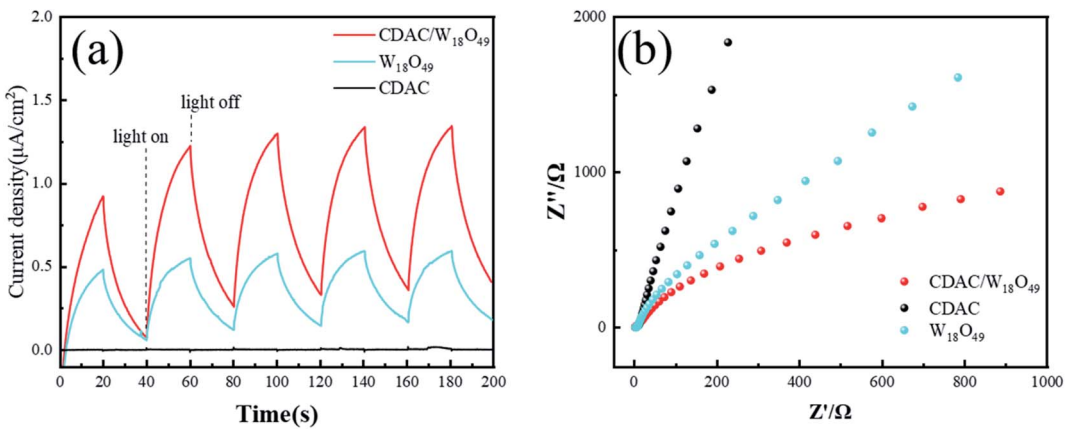

Fig. 7 (a) Photocurrent response of $W_{18}O_{49}$ nanowires CDAC and CDAC/$W_{18}O_{49}$. (b) Electrochemical impedance spectroscopy (EIS) of $W_{18}O_{49}$ nanowires CDAC and CDAC/$W_{18}O_{49}$ composites.

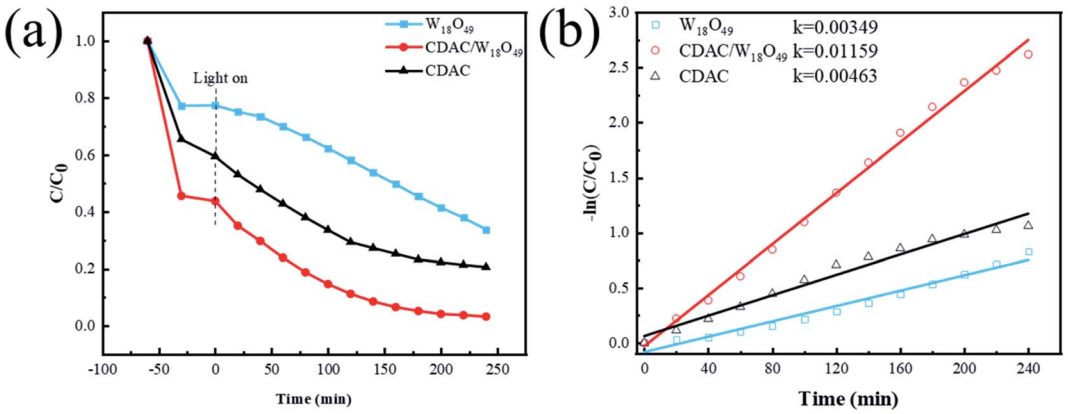

Fig. 8 (a) Photocatalytic degradation of MB with different samples under full-spectra light irradiation (λ > 365 nm) and (b) the corresponding pseudo-first-order kinetic plots.

radicals, with EDTA-2Na, *t*-BuOH and BQ as hole (h^+), hydroxyl radical ($^{\bullet}OH$) and superoxide radical ($^{\bullet}O_2^-$) trapping agents, respectively. As shown in the Fig. 10, when 1 μM 1,4-benzoquinone (BQ) was added to the reaction system, the photocatalytic degradation efficiency of MB under full-spectrum light irradiation (λ > 365 nm) was somewhat suppressed, indicating that superoxide radicals ($^{\bullet}O_2^-$) play some roles in the photocatalytic degradation process. The photocatalytic activity of CDAC/$W_{18}O_{49}$ composites was significantly reduced when 1 μM *tert*-butanol (*t*-BuOH) was added, which indicated that hydroxyl radicals (–OH) played a major role in the photocatalytic degradation process. In contrast, the degradation rate of MB was significantly increased by adding 1 μM disodium ethylenediaminetetraacetate (EDTA-2Na). The reason why EDTA-2Na can improve the degradation rate is that it can trap the hole (h^+), so that more $^{\bullet}O_2^-$ and $^{\bullet}OH$ reactive substances in the system can participate in the reaction, thus improving the degradation rate of MB.

In summary, a possible mechanism for the photocatalytic degradation of methylene blue (MB) by CDAC/$W_{18}O_{49}$ composite is proposed. As shown in Fig. 11 under full-spectrum light irradiation, $W_{18}O_{49}$ can absorb enough energy to generate excited electrons and form electron–hole pairs. The excited electrons in the conduction band (CB) of $W_{18}O_{49}$ can migrate smoothly into the CDAC due to the high conductivity and good electron storage capacity of CDAC, as evidenced by the photocurrent response and EIS. Thus, the combination of photogenerated carriers can be effectively suppressed and the absorption of visible light can be increased. The photo-induced electrons can react with oxygen and water adsorbed on the surface to generate $^{\bullet}O_2^-$ and $^{\bullet}OH$, which make great contribution on degradation of MB.[43] The porous structure and large specific surface area of CDAC can adsorb and enrich MB, and increase the concentration of MB in the composite, thus increasing the substrate concentration in the photocatalytic reaction region.[44] Thus, the synergistic effect of effective charge

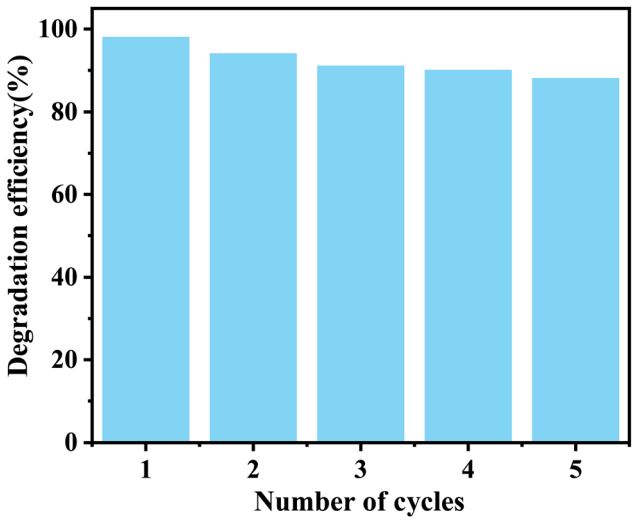

Fig. 9 Recyclability tests of CDAC/$W_{18}O_{49}$ composites in degradation of MB dye.

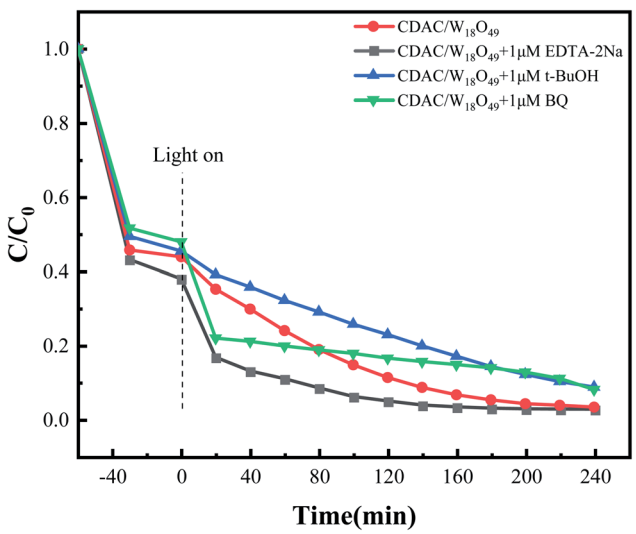

Fig. 10 Trapping experiments for the photocatalytic degradation of MB under full-spectra light irradiation (λ > 365 nm).

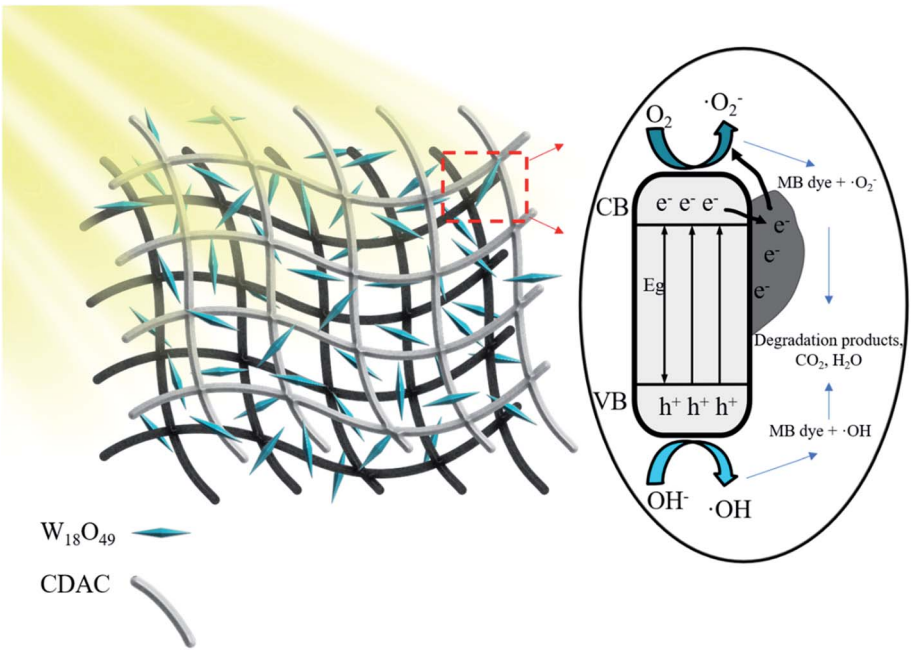

Fig. 11 Schematic illustration of the proposed reaction mechanism based on CDAC/$W_{18}O_{49}$ composite under full-spectrum light (λ > 365 nm).

separation, increased specific surface area, more light absorption and higher local MB concentration improves the photocatalytic activity of CDAC/$W_{18}O_{49}$ composites.

4. Conclusions

In conclusion, CDAC/$W_{18}O_{49}$ composites were synthesized by successfully assembling $W_{18}O_{49}$ nanowires onto CDAC prepared using KOH-active cow dung by co-hydrothermal treatment. The prepared CDAC/$W_{18}O_{49}$ composites showed higher photocatalytic activity and removal rate than pristine $W_{18}O_{49}$ nanowires in the full spectrum for MB. The large specific surface area and porous structure of CDAC in CDAC/$W_{18}O_{49}$ composites provide the $W_{18}O_{49}$ nanowires to absorb energy-generated excited electrons, which prolong the current load sub-life and accelerate the charge transfer; meanwhile, CDAC enhances the adsorption capacity of the composites to MB, thus improving the photocatalytic activity. Therefore, the prepared CDAC/$W_{18}O_{49}$ composite is an effective material for the photocatalytic degradation of methylene blue (MB).

Conflicts of interest

There are no conflicts to declare.

Acknowledgements

This work was supported by National Natural Science Foundation (No. 51972068), Natural Science Foundation of Guangxi Province (No. 2021GXNSFBA076003) and Guangxi Key Laboratory of Manufacturing Systems and Advanced Manufacturing Technology (20-065-40S007).

References

1 B. Yang, W. Li, M. Zhang, L. Wang and X. Ding, *ACS Nano*, 2021, **15**, 7195–7207.
2 P. Wang, P. Wang, Y. Guo, L. Rao and C. Yan, *Chem. Eng. J.*, 2021, 412.
3 R. K. Sonwani, G. Swain, B. S. Giri, R. S. Singh and B. N. Rai, *Bioresour. Technol.*, 2020, **302**, 122811.
4 N. Mohammed, H. Lian, M. S. Islam, M. Strong, Z. Shi, R. M. Berry, H.-Y. Yu and K. C. Tam, *Chem. Eng. J.*, 2021, 417.
5 S. Rojas and P. Horcajada, *Chem. Rev.*, 2020, **120**, 8378–8415.
6 E. Routoula and S. V. Patwardhan, *Environ. Sci. Technol.*, 2020, **54**, 647–664.
7 A. A. Alqadami, M. Naushad, Z. A. Alothman and T. Ahamad, *J. Environ. Manage.*, 2018, **223**, 29–36.
8 P. Khare, A. Singh, S. Verma, A. Bhati, A. K. Sonker, K. M. Tripathi and S. K. Sonkar, *ACS Sustainable Chem. Eng.*, 2017, **6**, 579–589.
9 W. Lü, Y. Wu, J. Chen and Y. Yang, *CrystEngComm*, 2014, **16**, 609–615.
10 E. Forgacs, T. Cserhati and G. Oros, *Environ. Int.*, 2004, **30**, 953–971.
11 R. A. Pereira, M. F. R. Pereira, M. M. Alves and L. Pereira, *Appl. Catal., B*, 2014, **144**, 713–720.
12 Z. Gan, A. Zhao, M. Zhang, W. Tao, H. Guo, Q. Gao, R. Mao and E. Liu, *Dalton Trans.*, 2013, **42**, 8597–8605.
13 S. H. Chang, *Environ. Sci. Pollut. Res. Int.*, 2020, **27**, 32371–32388.
14 K. Paździor, L. Bilińska and S. Ledakowicz, *Chem. Eng. J.*, 2019, 376.
15 M. Kamali, L. Appels, E. E. Kwon, T. M. Aminabhavi and R. Dewil, *Chem. Eng. J.*, 2021, 420.

16 Y. Deng, L. Tang, C. Feng, G. Zeng, Z. Chen, J. Wang, H. Feng, B. Peng, Y. Liu and Y. Zhou, *Appl. Catal., B*, 2018, **235**, 225–237.
17 N. Zhang, C. Chen, Z. Mei, X. Liu, X. Qu, Y. Li, S. Li, W. Qi, Y. Zhang, J. Ye, V. A. Roy and R. Ma, *ACS Appl. Mater. Interfaces*, 2016, **8**, 10367–10374.
18 X. Li, S. Yang, J. Sun, P. He, X. Xu and G. Ding, *Carbon*, 2014, **78**, 38–48.
19 G. T. Phan, D. V. Pham, R. A. Patil, C.-C. Lai, W.-C. Yeh, Y. Liou and Y.-R. Ma, *Appl. Mater. Today*, 2019, **15**, 605–613.
20 N. Zhang, X. Li, Y. Liu, R. Long, M. Li, S. Chen, Z. Qi, C. Wang, L. Song, J. Jiang and Y. Xiong, *Small*, 2017, **13**, 1701354.
21 C. Zhu, S. Zheng, T. Cao, C. Lin and Z. Xie, *J. Nanoparticle Res.*, 2018, 20.
22 Z.-F. Huang, J.-J. Zou, L. Pan, S. Wang, X. Zhang and L. Wang, *Appl. Catal., B*, 2014, **147**, 167–174.
23 X. Li, J. Yu and M. Jaroniec, *Chem. Soc. Rev.*, 2016, **45**, 2603–2636.
24 Y. Zhang, Y. W. Tan, H. L. Stormer and P. Kim, *Nature*, 2005, **438**, 201–204.
25 M. J. Allen, V. C. Tung and R. B. Kaner, *Chem. Rev.*, 2010, **110**, 132–145.
26 H. Huang, Z. Yue, G. Li, X. Wang, J. Huang, Y. Du and P. Yang, *J. Mater. Chem. A*, 2013, **1**, 15110–15116.
27 T. Do Minh, J. Song, A. Deb, L. Cha, V. Srivastava and M. Sillanpää, *Chem. Eng. J.*, 2020, 394.
28 A. Khataee, B. Kayan, P. Gholami, D. Kalderis and S. Akay, *Ultrason. Sonochem.*, 2017, **39**, 120–128.
29 D. W. Cho, K. Yoon, Y. Ahn, Y. Sun, D. C. W. Tsang, D. Hou, Y. S. Ok and H. Song, *J. Hazard. Mater.*, 2019, **374**, 412–419.
30 J. R. Kim and E. Kan, *J. Environ. Manage.*, 2016, **180**, 94–101.
31 K. B. Cantrell, T. Ducey, K. S. Ro and P. G. Hunt, *Bioresour. Technol.*, 2008, **99**, 7941–7953.
32 D. Bhattacharjya and J.-S. Yu, *J. Power Sources*, 2014, **262**, 224–231.
33 P. Zhang, Y. Li, Y. Cao and L. Han, *Bioresour. Technol.*, 2019, **285**, 121348.
34 M. Thommes, K. Kaneko, A. V. Neimark, J. P. Olivier, F. Rodriguez-Reinoso, J. Rouquerol and K. S. W. Sing, *Pure Appl. Chem.*, 2015, **87**, 1051–1069.
35 X. Chang, L. Dong, Y. Yin and S. Sun, *RSC Adv.*, 2013, **3**, 15005–15013.
36 D. Y. Lu, J. Chen, J. Zhou, S. Z. Deng, N. S. Xu and J. B. Xu, *J. Raman Spectrosc.*, 2007, **38**, 176–180.
37 N. Lu, Z. Zhang, Y. Wang, B. Liu, L. Guo, L. Wang, J. Huang, K. Liu and B. Dong, *Appl. Catal., B*, 2018, **233**, 19–25.
38 Z. Lou, Q. Gu, L. Xu, Y. Liao and C. Xue, *Chem.–Asian J.*, 2015, **10**, 1291–1294.
39 Y. Ou, G. Zhu, W. Zhang, S. Zhang, J. Gao, H. Lu, G. Li, Y. Huang and M. Hojamberdiev, *Sens. Actuators, B*, 2021, 347.
40 P. Ranjith, S. Sreevalsa, J. Tyagi, K. Jayanthi, G. Jagannath, P. Patra, S. Ahmad, K. Annapurna, A. R. Allu and S. Das, *J. Alloys Compd.*, 2020, 826.
41 H. Cheng, T. Kamegawa, K. Mori and H. Yamashita, *Angew. Chem., Int. Ed.*, 2014, **53**, 2910–2914.
42 J. Yan, T. Wang, G. Wu, W. Dai, N. Guan, L. Li and J. Gong, *Adv. Mater.*, 2015, **27**, 1580–1586.
43 B. Bhuyan, B. Paul, S. S. Dhar and S. Vadivel, *Mater. Chem. Phys.*, 2017, **188**, 1–7.
44 X. Li, X. Qian, X. An and J. Huang, *Appl. Surf. Sci.*, 2019, **487**, 1262–1270.